

Accessing the anisotropic non-thermal phonon populations in black phosphorus

Hélène Seiler,^{1,*} Daniela Zahn,¹ Marios Zacharias,^{1,2} Patrick Hildebrandt,¹ Thomas Vasileiadis,¹ Yoav William Windsor,¹ Yingpeng Qi,¹ Christian Carbogno,¹ Claudia Draxl,³ Fabio Caruso,^{3,4} and Ralph Ernstorfer^{1,†}

¹*Fritz Haber Institute of the Max Planck Society, 14195 Berlin, Germany*

²*Department of Mechanical and Materials Science Engineering,*

Cyprus University of Technology, P.O. Box 50329, 3603 Limassol, Cyprus

³*Institut für Physik and IRIS Adlershof, Humboldt-Universität zu Berlin, Berlin, Germany*

⁴*Institut für Theoretische Physik und Astrophysik,*

Christian-Albrechts-Universität zu Kiel, D-24098 Kiel, Germany

(Dated: October 12, 2021)

Microscopic scattering processes in solids are governed by the symmetry and anisotropy of the electronic and phononic structures. Femtosecond electron inelastic scattering experiments reveal a momentum-resolved picture of transient anisotropic phonon populations in photoexcited black phosphorus. Based on many-body calculations of the electron-phonon and phonon-phonon interactions, we developed an approach to predict the influence of the non-equilibrium lattice dynamics on the structure factor. By directly comparing the experimental and calculated structure factors, we demonstrate that the anisotropic conduction band is at the origin of the non-thermal phonon population and that our model reproduces the subsequent lattice thermalization.

Black phosphorus (BP) has recently received significant attention for its potential applications in optoelectronic devices [1–5]. In addition to its tunable bandgap in the mid-IR [2, 5, 6] and high carrier mobility [1, 3, 7], a defining feature of BP is the pronounced crystalline anisotropy of its layered structure. This gives rise to a variety of anisotropic macroscopic properties, such as thermal [8–10] and electrical conductivities [2, 3, 11, 12] as well as optical properties [3, 13–15]. These are governed by complex microscopic interactions between the electrons and the phonons, as well as between the phonons themselves. Despite recent progress in measuring carrier dynamics in BP [12, 16–18], a detailed understanding of these microscopic interactions remains difficult, as it requires accessing the relevant scattering processes with time, momentum, and energy resolution. In addition, anisotropy can manifest itself on several levels, from the electronic and vibrational properties to electron-phonon and phonon-phonon interactions. Disentangling these contributions in non-equilibrium situations is therefore particularly challenging for anisotropic materials.

In a recent work, some of us have shown that non-thermal phonon distributions persist for tens of picoseconds in BP [19]. Here, we perform femtosecond electron inelastic scattering (FEIS) experiments to reveal the microscopic origins of this non-thermal behavior with momentum resolution. We show that the anisotropic conduction band of BP profoundly influences the decay path of photoexcited carriers, and it underpins the formation of a non-thermal anisotropic phonon population. Several recent approaches have been implemented to model non-thermal phonon distributions [20–24]. In this work, we propose a new approach that combines a non-thermal

lattice model obtained from first-principles calculations of electron-phonon and phonon-phonon couplings with computations of the one-phonon structure factor. By directly comparing experimental with calculated signals, we establish a microscopic thermalization picture of the anisotropic non-thermal phonon populations in photoexcited BP.

BP crystallizes in a layered orthorhombic structure (space group 64) [26]. The in-plane *armchair* and *zigzag* directions are shown in Fig. 1(a). To investigate how BP thermalizes following photoexcitation with momentum and time resolutions, we perform FEIS measurements on a free-standing thin film of BP with an estimated thickness of 39 ± 5 nm, obtained by mechanical exfoliation of a bulk crystal. A schematic illustration of the experiment is shown in Fig. 1(b). We employ an optical laser pulse to drive electronic excitations, followed by an electron probe pulse which diffracts off the lattice at a later time, providing a direct probe of atomic motions in momentum space [27]. All measurements are performed at 100 K. An exemplary static diffraction pattern of BP is seen in Fig. 1(c), consistent with previous TEM works [28]. Specifically, the BP flake is excited with a light pulse polarized along the *armchair* direction with 1.61 eV photon pulse energy (0.59 eV pump results are also available in the Supplemental Material [29]). The resulting estimated initial carrier density is $n_e \simeq 1.4 \cdot 10^{21}$ electrons/cm³ [29].

The electronic band structure of BP, calculated with density-functional theory, is shown in Fig. 1(d), consistent with previous works [30, 31]. The high-symmetry points in the Brillouin zone (BZ) are indicated in Fig. 1(e) and follow the labeling convention of Ref. [26]. Remarkable signatures of anisotropy can be observed in the electronic properties. The conduction band is characterized by pockets that are located at Z and close to Y, A and A' high-symmetry points, but there are no pockets along the Γ -X and Z-Q directions. The optical excitation drives vertical transitions in the vicinity of the Z point, impul-

* corresponding author: seiler@fhi-berlin.mpg.de

† corresponding author: ernstorfer@fhi-berlin.mpg.de

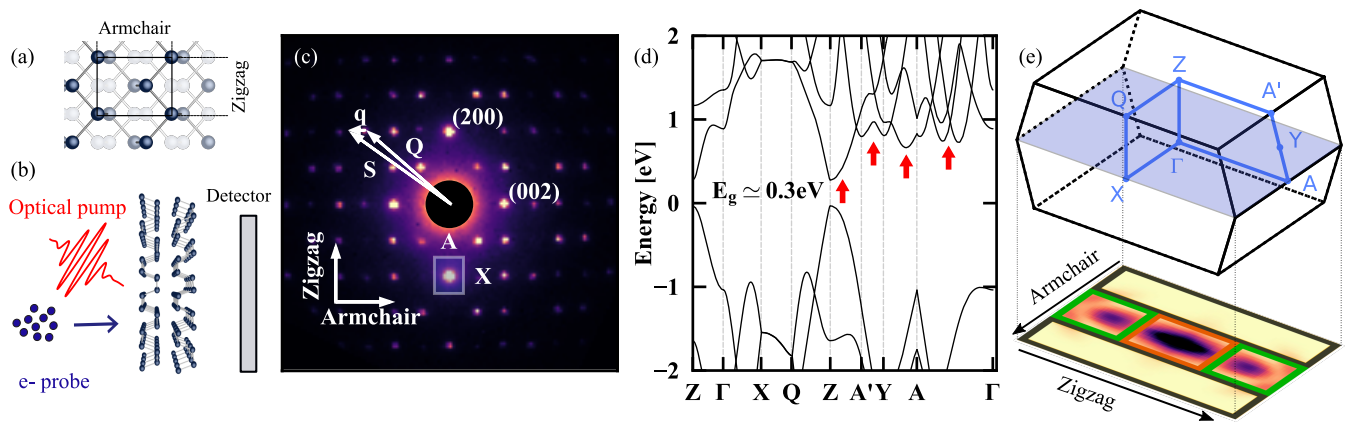


FIG. 1. (a) In-plane atomic structure of BP. (b) Schematic illustration of femtosecond electron scattering. (c) Exemplary transmission diffraction pattern of BP. First Brillouin zones can be drawn around each Bragg reflection, as illustrated by a rectangle over the $(\bar{2}00)$ reflection. An arbitrary position in reciprocal space, \mathbf{S} , can always be expressed as $\mathbf{G} + \mathbf{q}$, where \mathbf{G} is a reciprocal lattice vector defined by the Miller indices and \mathbf{q} the phonon wavevector. (d) Electronic band structure calculated from density-functional theory in the PBE approximation [25]. The conduction bands were shifted by 0.2 eV in energy to match the experimentally observed bandgap of $E_g \simeq 0.3$ eV. (e) Brillouin zone with labeling of high-symmetry points. Our FEIS experiments probe the blue plane. Below, the momentum distribution of photoexcited carriers approximated by a Fermi-Dirac function $f_{n\mathbf{k}}$ is shown (dark regions: more excited carriers). The colored rectangles indicate phonons groups, see text.

sively generating a non-equilibrium electron population in the conduction band. Considering our pump photon energy, one can expect intravalley scattering processes within the Z pocket to play an important role in the relaxation dynamics towards the conduction band minimum through emission of low-wavevector phonons. Intervalley scattering pathways can also transfer electrons to the neighboring Y, A and A' valleys along the *zigzag* direction. First insight into the non-equilibrium dynamics of the crystal lattice is obtained from the dynamics of the Bragg reflections. The anisotropic lattice dynamics of BP is reflected in the time evolution of the elastic scattering signals, shown in Fig. 2(a) and described in detail in Ref. [19]. Briefly, the dynamics of both *armchair* and *zigzag* reflections are well-captured by bi-exponential decays, with fast time constants of around 500 fs and slower time constants of approximately 20 ps.

Here, we go beyond the analysis of the elastic scattering signals and phonon-averaged structural dynamics towards a more detailed picture of lattice relaxation. This can be obtained by investigating the inelastic scattering signals around specific Bragg reflections, shown for selected high-symmetry points in Fig. 2 (b). The diffraction pattern can be divided into BZs around each Bragg reflection, as illustrated in Fig. 1 (c) for the $(\bar{2}00)$ reflection. As inelastic scattering occurs primarily through scattering off of phonons, the signal measured at a given point in the BZ reflects phonon populations with the same momentum [20, 21, 33–36]. The red curve in Fig. 2 (b) represents the relative intensity of the FEIS signal as a function of time at the A point. Similar dynamics are observed at all the investigated A points. A bi-exponential fit to the data yields a rising time constant of 1.7 ± 0.1 ps, followed by a slower relaxation of $30 \pm$

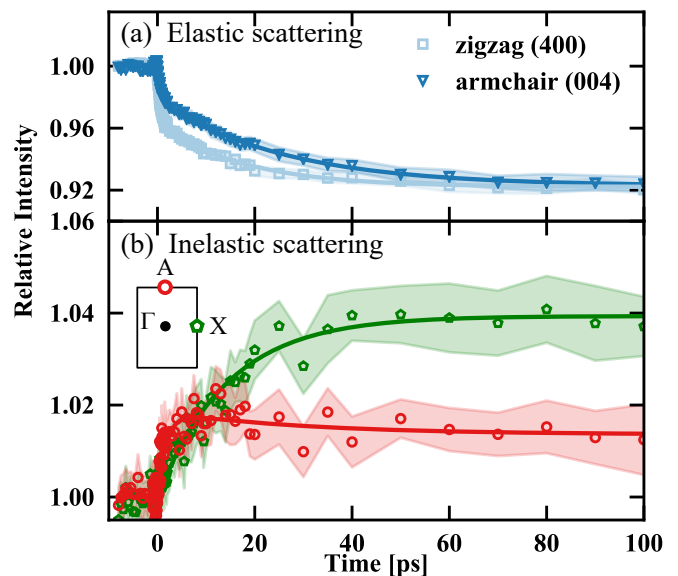


FIG. 2. (a) Exemplary anisotropic elastic scattering signals for *zigzag* (squares) and *armchair* reflections (triangles). (b) Inelastic scattering signal at A (circles) and X (pentagons) around the 400 reflection. The data in both panels is the average over the Friedel pair (e.g. (400) and $(\bar{4}00)$). The error estimates represent the standard error of the mean signal over multiple delay scans.

2 ps. We note that the 1.7 ps time constant does not appear in an elastic scattering analysis. The green curve in Fig. 2 (b) shows the time evolution of the inelastic signal at the X point. The phonon dynamics at the X point drastically differs from that at the A point. We find the best fit to be a mono-exponential rise function with a

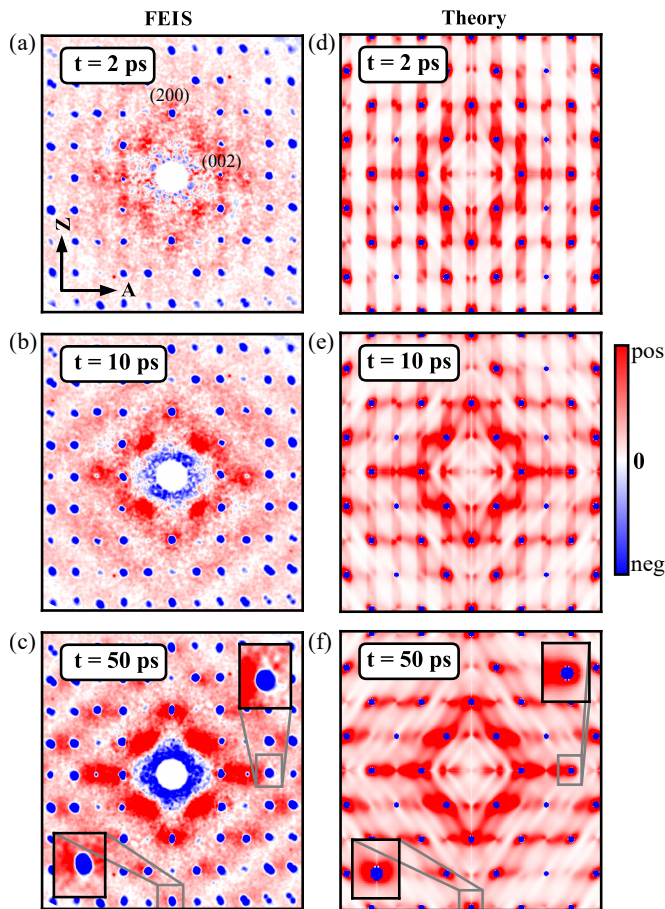


FIG. 3. (a-c) Momentum-resolved electron diffraction signals, $I(\mathbf{S}, t) - I(\mathbf{S}, t < t_0)$, at pump-probe delays of 2 ps, 10 ps, and 50 ps. Two-fold symmetrized data [32], raw data shown in Supplemental Material [29]. The Bragg reflections (blue dots) are negative due to the Debye-Waller effect. The inelastic background (red) qualitatively evolves as a function of pump-probe delay. Selected Brillouin zones are shown in inset for the (004) and the $(\bar{4}00)$ reflections on the 50 ps map. All data are normalized to a common number. (d-f) Simulated non-equilibrium scattering signals at pump-probe delays of 2 ps, 10 ps, and 50 ps. The phonon temperatures are based on the non-thermal model described in the text and shown in Fig. 4 (a). All data are normalized to a common number.

time constant of 14.3 ± 0.1 ps. These measurements reveal that phonon excitations following photoexcitation are highly momentum-dependent in BP.

A comprehensive view of transient phonon distributions in momentum space is shown in Figs. 3 (a-c), at pump-probe delays of 2 ps, 10 ps, and 50 ps. These data demonstrate profound, qualitative changes in the inelastic scattering signal as pump-probe delay increases, reflecting different phonon populations at different times. While the inelastic pattern at 2 ps is weak and displays faint lines in the Γ -A direction, the inelastic signal at 50 ps is much stronger, of a different shape, and more anisotropic. A closer inspection of the changes in inelastic scattering signal around Bragg reflections,

shown as insets in Fig. 3 (c), reveals high anisotropy between the intensities along the two main crystal axes at 50 ps. These highly anisotropic dynamics within a given BZ, and between BZs, highlight the value of time-resolved inelastic scattering as direct probes of transient non-thermal phonon distributions in momentum space [Figs. 3 (a-c)].

To gain further microscopic insight from these observations, we theoretically describe the carrier and vibrational dynamics of photoexcited BP. Following photoexcitation and Auger thermalization, the distribution of photoexcited carriers may be approximately described by the Fermi-Dirac function $f_{n\mathbf{k}} = [e^{(\varepsilon_{n\mathbf{k}} - \mu(T_{\text{el}}))/k_{\text{B}}T_{\text{el}}} + 1]^{-1}$ with an effective temperature T_{el} ($\varepsilon_{n\mathbf{k}}$ is the conduction band energy). The effective chemical potential, $\mu_{\text{eff}}(T_{\text{el}})$, is directly related to the density of photoexcited carriers via the relation $N = \Omega_{\text{BZ}}^{-1} \int d\mathbf{k} f_{n\mathbf{k}}(\mu_{\text{eff}}, T_{\text{el}})$. For our experimental density of photoexcited carriers, $N = 1.4 \cdot 10^{21} \text{ cm}^{-3}$, the effective chemical potential $\mu_{\text{eff}}(T_{\text{el}} = 0)$ is 0.12 eV above the conduction band minimum. The 2D calculated electron distribution is shown under the BZ in Fig. 1 (e) for $T_{\text{el}} = 2000$ K. It indicates that carriers have a highly anisotropic distribution of crystal momenta resulting from the partial filling of the pockets indicated in Fig. 1 (d). Owing to momentum conservation, one may expect the relaxation of carriers to the conduction band minimum (located at the Z point) to entail a predominant emission of phonons with momenta \mathbf{q} along the Z-Y, Z-A' and Z-A directions, leading to a long-lived anisotropy in the phonon population across the BZ.

To investigate possible signatures of these phenomena on the FEIS signals, we define a phenomenological model of carrier thermalization, which explicitly accounts for the anisotropic scattering phase space in the BZ. In the two-temperature model (TTM) [37, 38], and its generalization to multiple temperatures [20, 22–24, 39–41], the temporal evolution of the electron and phonon distribution functions for a photoexcited system are determined via a set of coupled equations for the effective electron and phonon temperature, T_{el} and T_{ph} , respectively. Here, we generalize this model to account for momentum anisotropy of the initial electronic population. Specifically, we group phonons based on scattering phase space constraints dictated by the initial excitation fluence and the shape of the electronic band structure. The BZ is partitioned in three rectangular cuboids, which projections are shown as the colored rectangles in Fig. 1 (e): the Z region (orange rectangle), that includes the Z pocket, the Y region (green rectangles), that includes the Y, A, and A' pockets, and the X region (dark grey rectangles). The effective temperature T_{ν} for the phonons with momentum in the ν -th region is determined through the time-propagation of the coupled equations in a non-thermal lattice model (NLM) [21, 24]. This approach, while partially phenomenological, includes first-principles computations of the electron-phonon, [42–45] and phonon-phonon [46, 47] interactions. More details

are given in the Supplemental Material [29]. Importantly, our calculations do not indicate strong signatures of anisotropy in the electron-phonon and phonon-phonon coupling constants themselves. Instead, the evolution of the non-thermal populations seems mostly governed by the anisotropic phase space.

The effective temperatures extracted from the model are shown in Fig. 4(a). The photoexcitation of the electrons at $t = 0$, marked by the peak of T_{el} , is followed by a sharp increase in the effective temperature for phonons in the Y and Z regions. The slower increase of T_{ν} in the X region reflects the low emission rate for phonons with momenta in this region, owing to the lack of available electronic transitions. At longer timescales, phonon-phonon scattering leads to a thermalization of the phonon population, reflected by the different effective temperatures approaching a single value. While the phonon-phonon thermalization timescales match the experimental ones, the electron-phonon equilibration from the model occurs significantly faster than in the experiment. This results from an overestimation of the electronic relaxation at early times by any multi-temperature model, as pointed out recently [23]. Keeping this in mind, these theoretical results confirm that carrier relaxation in BP leads to the establishment of a highly anisotropic non-thermal phonon population persisting for tens of picoseconds.

The predictive power of our model is assessed by combining the calculated temperatures with calculations of the zero-phonon and one-phonon contributions to the structure factor signals [48, 49]. Such calculations have been previously employed to describe thermal diffuse scattering (TDS) experiments [50, 51]. The harmonic one-phonon contribution to the structure factor at temperature T is given by [52]:

$$I_1(\mathbf{S}, T) = N_p |f(\mathbf{S})|^2 \sum_{\kappa\kappa'} \frac{M_0}{\sqrt{M_{\kappa} M_{\kappa'}}} e^{-W_{\kappa\kappa'}(\mathbf{S}, T)} \quad (1)$$

$$\times \sum_{\nu\alpha\alpha'} S_{\alpha} S_{\alpha'} \text{Re} \left[e_{\kappa\alpha}^{\nu}(\mathbf{S}) e_{\kappa'\alpha'}^{\nu*}(\mathbf{S}) \right] \cos(\mathbf{S} \cdot \mathbf{R}_{\kappa\kappa'}) \langle u_{\mathbf{S}\nu}^2 \rangle_T.$$

Here N_p is the number of points used to integrate over the first BZ, $f(\mathbf{S})$ the atomic scattering factor, M_{κ} the mass of atom κ , M_0 the proton mass, $\mathbf{R}_{\kappa\kappa'} = \mathbf{R}_{\kappa} - \mathbf{R}_{\kappa'}$ the vector connecting two atoms in the unit cell, and $W_{\kappa\kappa'}(\mathbf{S}, T)$ the exponent of the Debye-Waller factor [29]. The phonon polarization vector of the normal mode with wavevector \mathbf{S} , branch index ν , and frequency $\Omega_{\mathbf{S}\nu}$ is denoted as $\mathbf{e}_{\kappa}^{\nu}(\mathbf{S})$ with Cartesian components $e_{\kappa\alpha}^{\nu}(\mathbf{S})$. The mean-squared displacement of the atoms due to mode $\mathbf{S}\nu$ is defined as $\langle u_{\mathbf{S}\nu}^2 \rangle_T = \hbar / (2M_0\Omega_{\mathbf{S}\nu}) [2n_{\mathbf{S}\nu}(T) + 1]$, where $n_{\mathbf{S}\nu}(T)$ represents the Bose-Einstein occupation factor.

The time-dependence of the one-phonon structure factor is encoded in $\langle u_{\mathbf{S}\nu}^2 \rangle_T$, which is directly related to phonon populations $n_{\mathbf{S}\nu}(T)$. Writing the structure factor in its expanded form given by Eq. (1) allows for its decomposition into *self* ($\kappa = \kappa'$) and *distinct* ($\kappa \neq \kappa'$) scattering contributions [53]. We find that the interference structure observed in the experimental signals

are caused by the distinct contributions (Supplemental Material [29]). To account for the influence of a non-equilibrium lattice dynamics on the FEIS map, we evaluated Eq. (1) at each time snapshot by populating phonons according to the model temperatures illustrated in Fig. 4 (a). The calculated non-equilibrium one-phonon structure factor intensity at 2 ps is shown in Fig. 3 (d), using the TDS signal at 100 K as reference. In this highly non-equilibrium situation, our model provides qualitative agreement with the experimental pattern in Fig. 3 (a). In particular, the higher number of phonons along the Γ -A path compared to the Γ -X path is captured by our momentum-resolved non-thermal lattice model. The calculated inelastic scattering intensities at 10 ps and 50 ps are shown in Fig. 3 (b) and (c), respectively.

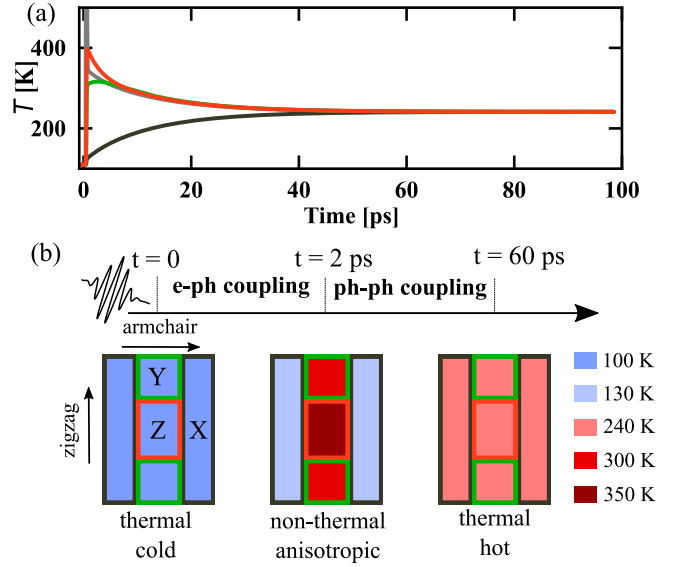


FIG. 4. (a) Time-evolution of the temperatures of the three phonon groups (Z: orange, Y: green, X: dark grey) and the electrons (light grey) based on the non-thermal lattice model. (b) Cartoon representation of thermalization steps in photoexcited BP, highlighting how different parts of the Brillouin zone heat up as a function of time.

Bringing the various pieces of information together, we establish the following picture for lattice thermalization in BP following photoexcitation, summarized in the cartoon in Fig. 4(b): After the electrons are impulsively excited by the laser pulse, they undergo Auger scattering and thermalize to a Fermi-Dirac distribution. This yields a highly anisotropic distribution of photoexcited carrier momenta, predominantly populating the Z, Y, A, and A' pockets. Subsequently, two types of electron-phonon scattering pathways exist. First, efficient intravalley scattering occurs with low-momenta phonons within the Z valley with a characteristic timescale of $\simeq 500$ fs. According to our first-principles calculations, both low-momenta acoustic and optical phonons possess similar coupling strength to the electrons. A second category of pathways involve electron scattering with high-momenta phonons

from the Z to the Y, A, and A' valleys, but also from these valleys back to the Z valley, with a timescale of $\simeq 2$ ps. Due to the higher number of optical phonon modes, we expect that these scattering events are mediated by high-momenta optical phonons. The phonon distribution resulting from electron-phonon scattering yields the non-equilibrium signatures seen at 2 ps in Fig. 3(b). These hot phonons subsequently thermalize with other phonons via phonon-phonon coupling, thereby bringing the lattice to a single common temperature within $\simeq 60$ ps [19]. The diffuse scattering intensity at 50 ps shown in Fig. 3(c) represents a hot, almost thermalized phonon population, dominated by acoustic phonons. The anisotropic phonon dispersion curve along the Γ -X versus Γ -Y paths is at the origin of the phonon-phonon scattering from the Γ -Y to the Γ -X path within a BZ [29].

In conclusion, we found highly anisotropic transient phonon populations in photoexcited BP through time- and momentum-resolved inelastic scattering experiments. We have introduced a non-thermal lattice model based on momentum-space partitioning which explicitly accounts for the scattering phase space of electrons and phonons. In combination with calculations of the one-phonon structure factor and first-principles calculations

of the microscopic couplings, this model successfully reproduces the time-dependent inelastic scattering maps and the phonon thermalization dynamics. In contrast to previous non-thermal lattice models for describing microscopic energy flow, where partitioning is based on the symmetry of phonons [20, 22, 41], we expect the notion of momentum-space partitioning introduced here to be an essential aspect of non-thermal lattice models for highly anisotropic crystals and composite materials like van der Waals heterostructures. This approach is fully transferable to near-equilibrium conditions as in thermal and electrical transport.

This work was funded by the Max Planck Society, the European Research Council (ERC) under the European Unions Horizon 2020 research and innovation program (Grant Agreement Number ERC-2015-CoG-682843), and partially by the Deutsche Forschungsgemeinschaft (DFG) - Projektnummer 182087777 - SFB 951. H.S. acknowledges support by the Swiss National Science Foundation under Grant No. P2SKP2-184100. Y.Q. acknowledges support by the Sino-German (CSC-DAAD) Postdoc Scholarship Program (Grant No. 57343410). We thank Maciej Dendzik for helpful discussions, and Laurent René de Cotret for his open-source software. F.C. and C.D. acknowledge Dino Novko for useful discussions.

-
- [1] L. Li, Y. Yu, G. J. Ye, Q. Ge, X. Ou, H. Wu, D. Feng, X. H. Chen, and Y. Zhang, *Nature Nanotechnology* **9**, 372 (2014).
- [2] J. Qiao, X. Kong, Z.-X. Hu, F. Yang, and W. Ji, *Nature Communications* **5**, 4475 (2014).
- [3] F. Xia, H. Wang, and Y. Jia, *Nature Communications* **5** (2014).
- [4] X. Ling, H. Wang, S. Huang, F. Xia, and M. S. Dresselhaus, *Proceedings of the National Academy of Sciences* **112**, 4523 (2015).
- [5] A. Castellanos-Gomez, *J. Phys. Chem. Lett.* **6**, 4280 (2015).
- [6] L. Li, J. Kim, C. Jin, G. J. Ye, D. Y. Qiu, F. H. da Jornada, Z. Shi, L. Chen, Z. Zhang, F. Yang, *et al.*, *Nature Nanotechnology* **12**, 21 (2016).
- [7] G. Long, D. Maryenko, J. Shen, S. Xu, J. Hou, Z. Wu, W. K. Wong, T. Han, J. Lin, Y. Cai, *et al.*, *Nano Letters* **16**, 7768 (2016).
- [8] S. Lee, F. Yang, J. Suh, S. Yang, Y. Lee, G. Li, H. Sung Choe, A. Suslu, Y. Chen, C. Ko, *et al.*, *Nature Communications* **6**, 8573 (2015).
- [9] Z. Luo, J. Maassen, Y. Deng, Y. Du, R. P. Garrelts, M. S. Lundstrom, P. D. Ye, and X. Xu, *Nature Communications* **6**, 8572 (2015).
- [10] H. Jang, J. D. Wood, C. R. Ryder, M. C. Hersam, and D. G. Cahill, *Advanced Materials* **27**, 8017 (2015).
- [11] H. Liu, A. T. Neal, Z. Zhu, Z. Luo, X. Xu, D. Tomnek, and P. D. Ye, *ACS Nano* **8**, 4033 (2014).
- [12] J. He, D. He, Y. Wang, Q. Cui, M. Z. Bellus, H.-Y. Chiu, and H. Zhao, *ACS Nano* **9**, 6436 (2015).
- [13] V. Tran, R. Soklaski, Y. Liang, and L. Yang, *Phys. Rev. B* **89**, 235319 (2014).
- [14] T. Low, A. S. Rodin, A. Carvalho, Y. Jiang, H. Wang, F. Xia, and A. H. Castro Neto, *Phys. Rev. B* **90**, 075434 (2014).
- [15] H. Jiang, H. Shi, X. Sun, and B. Gao, *ACS Photonics* **5**, 2509 (2018).
- [16] S. Ge, C. Li, Z. Zhang, C. Zhang, Y. Zhang, J. Qiu, Q. Wang, J. Liu, S. Jia, J. Feng, and D. Sun, *Nano Letters* **15**, 4650 (2015).
- [17] S. Roth, A. Crepaldi, M. Puppini, G. Gatti, D. Bugini, I. Grimaldi, T. R. Barrilot, C. A. Arrell, F. Frassetto, L. Poletto, *et al.*, *2D Materials* **6**, 031001 (2019).
- [18] Z. Chen, J. Dong, E. Papalazarou, M. Marsi, C. Giorgetti, Z. Zhang, B. Tian, J.-P. Rueff, A. Taleb-Ibrahimi, and L. Perfetti, *Nano Letters* **19**, 488 (2019).
- [19] D. Zahn, P.-N. Hildebrandt, T. Vasileiadis, Y. W. Windsor, Y. Qi, H. Seiler, and R. Ernstorfer, *Nano Letters* **20**, 3728 (2020).
- [20] L. P. R. de Cotret, J.-H. Pöhls, M. J. Stern, M. R. Otto, M. Sutton, and B. J. Siwick, *Physical Review B* **100**, (2019).
- [21] L. Waldecker, R. Bertoni, H. Huebener, T. Brumme, T. Vasileiadis, D. Zahn, A. Rubio, and R. Ernstorfer, *Phys. Rev. Lett.* **119** (2017).
- [22] L. Waldecker, R. Bertoni, R. Ernstorfer, and J. Vorberger, *Physical Review X* **6**, (2016).
- [23] S. Sadasivam, M. K. Y. Chan, and P. Darancet, *Phys. Rev. Lett.* **119**, 136602 (2017).
- [24] D. Novko, F. Caruso, C. Draxl, and E. Cappelluti, *Physical Review Letters* **124**, (2020).
- [25] J. P. Perdew, K. Burke, and M. Ernzerhof, *Physical Review Letters* **77**, 3865 (1996).
- [26] H. B. Ribeiro, M. A. Pimenta, and C. J. de Matos, *Jour-*

- nal of Raman Spectroscopy **49**, 76 (2018).
- [27] L. Waldecker, R. Bertoni, and R. Ernstorfer, *Journal of Applied Physics* **117**, 044903 (2015).
- [28] A. Castellanos-Gomez, L. Vicarelli, E. Prada, J. O. Island, K. L. Narasimha-Acharya, S. I. Blanter, D. J. Groenendijk, M. Buscema, G. A. Steele, J. V. Alvarez, *et al.*, *2D Materials* **1**, 025001 (2014).
- [29] See Supplemental Material at [URL].
- [30] S. Baroni, S. de Gironcoli, A. Dal Corso, and P. Giannozzi, *Rev. Mod. Phys.* **73**, 515 (2001).
- [31] P. Giannozzi, O. Andreussi, T. Brumme, O. Bunau, M. B. Nardelli, M. Calandra, R. Car, C. Cavazzoni, D. Ceresoli, M. Cococcioni, *et al.*, *Journal of Physics: Condensed Matter* **29**, 465901 (2017).
- [32] L. P. R. de Cotret, M. R. Otto, M. J. Stern, and B. J. Siwick, *Advanced Structural and Chemical Imaging* **4**, (2018).
- [33] M. J. Stern, L. P. R. de Cotret, M. R. Otto, R. P. Chate-lain, J.-P. Boisvert, M. Sutton, and B. J. Siwick, *Physical Review B* **97** (2018).
- [34] M. Trigo, J. Chen, V. H. Vishwanath, Y. M. Sheu, T. Graber, R. Henning, and D. A. Reis, *Phys. Rev. B* **82**, 235205 (2010).
- [35] M. Trigo, M. Fuchs, J. Chen, M. P. Jiang, M. Cam-marata, S. Fahy, D. M. Fritz, K. Gaffney, S. Ghimire, A. Higginbotham, *et al.*, *Nature Physics* **9**, 790 (2013).
- [36] S. Wall, S. Yang, L. Vidas, M. Chollet, J. M. Glow-*nia*, M. Kozina, T. Katayama, T. Henighan, M. Jiang, T. A. Miller, *et al.*, *Science* **362**, 572 (2018).
- [37] S. Anisimov, Bonch-Bruevich, El'yashevich, Imas, Pavlenko, and Romanov, *Sov. Phys.-Tech. Phys.* **11**, 945 (1967).
- [38] P. B. Allen, *Phys. Rev. Lett.* **59**, 1460 (1987).
- [39] D. Novko, J. C. Tremblay, M. Alducin, and J. I. Juaristi, *Phys. Rev. Lett.* **122**, 016806 (2019).
- [40] F. Caruso, D. Novko, and C. Draxl, *Phys. Rev. B* **101**, 035128 (2020).
- [41] S. Ono, *Transactions of the Materials Research Society of Japan* **44**, 51 (2019).
- [42] S. Ponc e, E. Margine, C. Verdi, and F. Giustino, *Comp. Phys. Commun.* **209**, 116 (2016).
- [43] F. Giustino, M. L. Cohen, and S. G. Louie, *Phys. Rev. B* **76**, 165108 (2007).
- [44] A. Eiguren and C. Ambrosch-Draxl, *Phys. Rev. Lett.* **101**, 036402 (2008).
- [45] F. Giustino, *Reviews of Modern Physics* **89** (2017).
- [46] D. A. Broido, M. Malorny, G. Birner, N. Mingo, and D. A. Stewart, *Applied Physics Letters* **91**, 231922 (2007).
- [47] A. Togo, L. Chaput, and I. Tanaka, *Phys. Rev. B* **91**, 094306 (2015).
- [48] A. A. Maradudin, E. W. Montroll, and G. H. Weiss, *The-ory of lattice dynamics in the harmonic approximation* (Academic Press, New York, 1963) p. 240.
- [49] G. Grosso and G. Pastori Parravicini, *Solid state physics*, 2nd ed. (Elsevier, Oxford, 2014).
- [50] M. Holt, Z. Wu, H. Hong, P. Zschack, P. Jemian, J. Tis-*chler*, H. Chen, and T.-C. Chiang, *Phys. Rev. Lett.* **83**, 3317 (1999).
- [51] R. Xu and T. C. Chiang, *Zeitschrift f ur Kristallographie* **220** (2005).
- [52] M. Born, *Reports on Progress in Physics* **9**, 294 (1942).
- [53] L. Van Hove, *Phys. Rev.* **95**, 249 (1954).

Supplemental Material:

Accessing the anisotropic non-equilibrium phonon populations in black phosphorus

Hélène Seiler,¹ Daniela Zahn,¹ Marios Zacharias,^{1,2} Patrick Hildebrandt,¹ Thomas Vasileiadis,¹ Yoav William Windsor,¹ Yingpeng Qi,¹ Christian Carbogno,¹ Claudia Draxl,³ Fabio Caruso,^{3,4} and Ralph Ernstorfer¹

¹*Fritz Haber Institute of the Max Planck Society, 14195 Berlin, Germany*

²*Department of Mechanical and Materials Science Engineering,
Cyprus University of Technology, P.O. Box 50329, 3603 Limassol, Cyprus*

³*Institut für Physik and IRIS Adlershof, Humboldt-Universität zu Berlin, Berlin, Germany*

⁴*Institut für Theoretische Physik und Astrophysik,
Christian-Albrechts-Universität zu Kiel, D-24098 Kiel, Germany*

I. ESTIMATION OF EXCITED CARRIER DENSITY

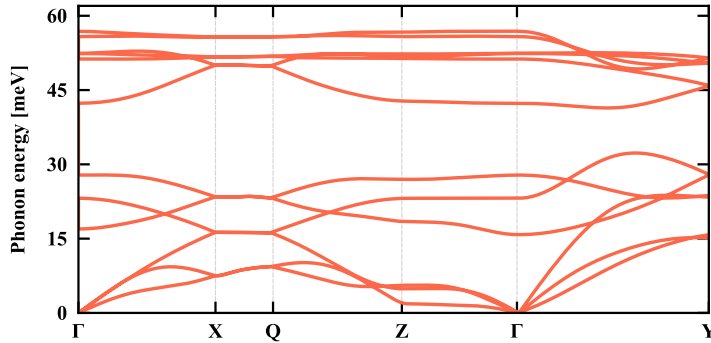
The incident fluence on the black phosphorus flake is $I_{\text{inc}} = 98 \text{ J/m}^2$. The complex refractive index of black phosphorus along the armchair direction at 800 nm is $3.19 + 0.29i$, as estimated from previous work [1]. We use transfer matrices to calculate the transmitted part, T , as well as the reflected part, R , of the incident fluence. This yields the absorbed fluence $I_{\text{abs}} = (1 - R - T) \cdot I_{\text{inc}}$. The carrier density per cubic centimeter is then:

$$n_e = 10^{-6} \cdot \frac{1}{E_{\text{ph}}} \cdot \frac{I_{\text{abs}}}{d} = 1.42 \cdot 10^{21} \text{ electrons/cm}^3,$$

where E_{ph} is the energy of one pump photon, and d is the flake thickness, which we estimate to $39 \pm 5 \text{ nm}$ based on transmission of the film and known optical constants [1].

II. PHONON BAND STRUCTURE

For the phonons simulations we employed the primitive cell of bulk black phosphorus (point group D_{2h} and space group Cmce) that contains 4 atoms [2]. Ab-initio calculations were performed using the PBE generalized gradient approximation [3] to density functional theory. We employed planewaves basis sets and Troullier-Martins norm-conserving pseudopotentials [4] as implemented in the **Quantum ESPRESSO** suite [5]. The planewaves kinetic energy cutoff was set to 90 Ry and the sampling of the Brillouin zone was performed using a uniform $12 \times 10 \times 10$ \mathbf{k} -point grid. We determine the interatomic force constants by means of density-functional perturbation theory calculations [6] using a $5 \times 5 \times 5$ Brillouin-zone \mathbf{q} -grid. The full set of phonon eigenmodes and eigenfrequencies was obtained by using standard Fourier interpolation of dynamical matrices on a $50 \times 50 \times 50$ \mathbf{q} -point grid. Such a dense grid guarantees a fine resolution of the calculated structure factor maps. The phonon band structure over a chosen high-symmetry path is shown in Supplementary Figure 1.



Supplementary Figure 1. Phonon dispersion of BP calculated from density-functional perturbation theory over the Γ -X-Q-Z- Γ -Y path.

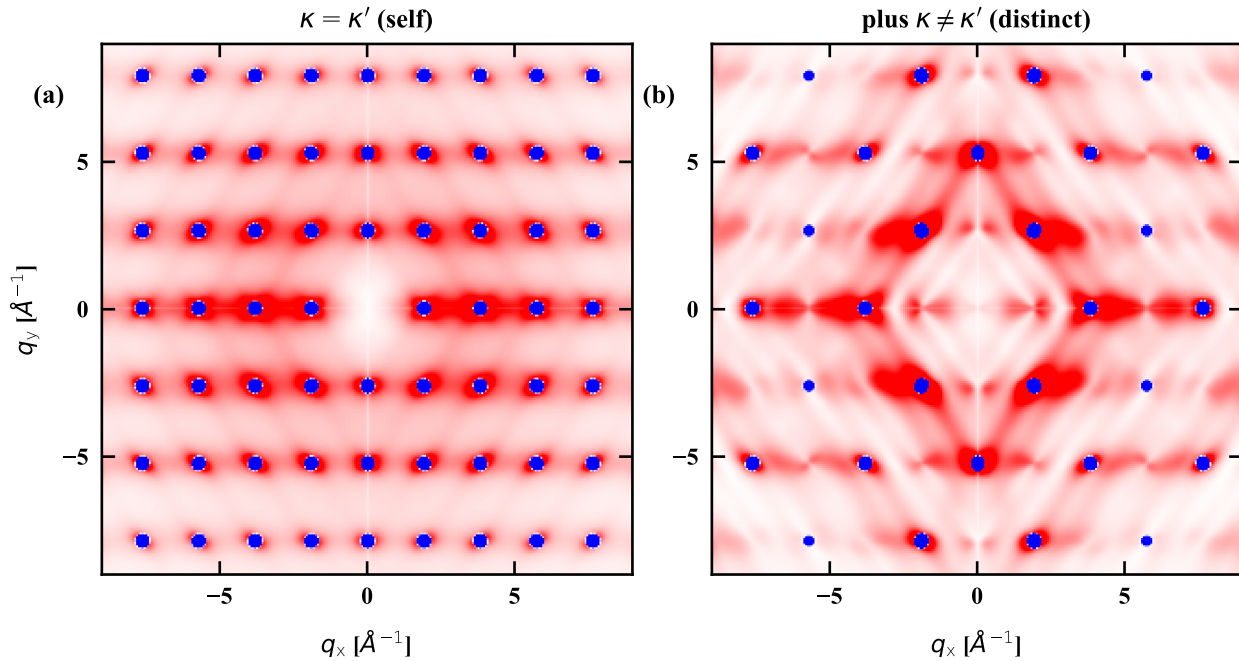
III. ONE-PHONON STRUCTURE FACTOR MAPS: EFFECTS OF CORRELATIONS

We use the expanded form of the one-phonon structure factor, displayed in Eq.(1) of the manuscript, to evaluate the influence of specific terms on the inelastic scattering intensity. For the atomic scattering factor $f(\mathbf{S})$ of BP we use the standard analytic expression expressed as a sum of Gaussian functions [7] using the parameters in Ref. [8]. The exponent of the Debye-Waller factor is given by $W_{\kappa\kappa'}(\mathbf{S}, T) = W_{\kappa}(\mathbf{S}, T) + W_{\kappa'}(\mathbf{S}, T)$, where [9]:

$$W_{\kappa}(\mathbf{S}, T) = \frac{M_0}{2N_p M_{\kappa}} \sum_{\mathbf{q}\nu} |\mathbf{S} \cdot \mathbf{e}_{\kappa}^{\nu}(\mathbf{q})|^2 \langle u_{\mathbf{q}\nu}^2 \rangle_T, \quad (1)$$

with all definitions given in the main text.

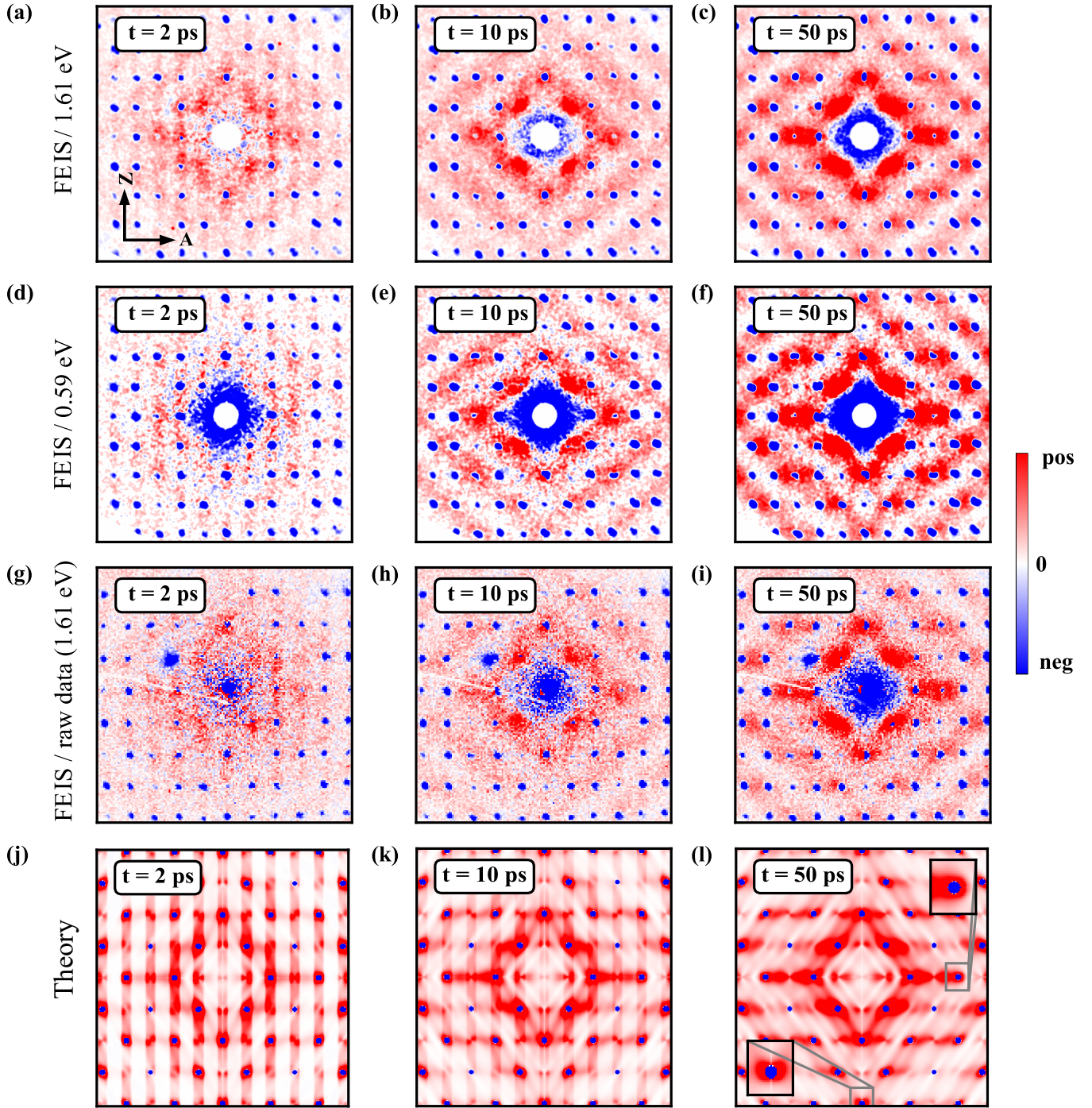
In supplementary Figure 2, we show computations of the structure factor when only self ($\kappa = \kappa'$) terms are taken into account, and when distinct ($\kappa \neq \kappa'$) scattering contributions are added. It is clear that including the distinct terms is paramount to reproduce the experimentally observed inelastic scattering signal.



Supplementary Figure 2. (a) One-phonon structure map when only self ($\kappa = \kappa'$) terms are accounted for. (b) One-phonon structure map when distinct ($\kappa \neq \kappa'$) terms are included. Both maps are obtained by computing $I_1(\mathbf{S}, T = 300 \text{ K}) - I_1(\mathbf{S}, T = 100 \text{ K})$.

IV. INELASTIC SCATTERING MAPS: RAW DATA AND INFLUENCE OF PUMP PHOTON ENERGY

In Supplementary Figure 3 we show a series of inelastic scattering maps at chosen delays and for different pump photon energies and/or data processing steps. Panels (a-c) and (j-l) correspond to the experimental and theoretical results shown in Figure 3 of the main text, respectively. They are reproduced here for convenience. Panels (d-f) display the inelastic scattering signals obtained when pumping the sample with 0.59 eV photons. The same initial excited electrons density is assumed for both the 0.59 eV and 1.61 eV experiments, based on the Bragg peaks' reduction at 300 ps. While the inelastic scattering signatures at 2 ps seem slightly more intense for the 1.61 eV pump, we observe the same qualitative thermalization process in both cases. Since the picosecond dynamics does not seem to depend significantly on the initial carrier distribution after excitation, the assumption of a thermalized electron system for our purposes seems justified. In the main text and in panels (a-f), we show two-fold symmetrized data. This processed data is obtained using the open-source Python environment developed by De Cotret et al. [10]. Prior to symmetrization, it was verified that the time-dependence of the elastic scattering for Friedel pairs showed the same dynamics within error margin. The raw data for the 1.61 eV pump are shown in panels (g-i).



Supplementary Figure 3. Inelastic scattering maps at 2 ps, 10 ps, and 50 ps for different pump photon energies and data processing steps. (a-c) Two-fold symmetrized, 1.61 eV pump. (d-f) Two-fold symmetrized, 0.59 eV pump. (g-i) Raw data (binned), 1.67 eV pump. (j-l) Theory results obtained assuming an excited carrier density of $1.42 \cdot 10^{21}$ electrons/cm³.

V. MOMENTUM-RESOLVED NON-THERMAL LATTICE MODEL

To describe the non-equilibrium dynamics of electrons and phonons in black phosphorus, we generalize the non-thermal lattice model to explicitly account for momentum resolution in the phonon population. In this model, the out-of-equilibrium occupation of electron energy levels in the conduction band are approximated by a Fermi-Dirac distribution function $f(\epsilon, \mu, T_{el}) = [e^{(\epsilon_{nk} - \mu(T_{el}))/k_B T_{el}} + 1]^{-1}$ with an effective temperature T_{el} , band energy ϵ_{nk} , and

chemical potential μ . We consider the effective chemical potential, μ_{eff} , with $\mu_{\text{eff}}(T_{\text{el}} = 0) = 0.12$ eV (energies are referenced to the conduction band minimum), which corresponds to the experimental density of photoexcited carriers $n = 1.4 \cdot 10^{21}$ cm $^{-3}$. To account for momentum anisotropy in the lattice dynamics, we divide the BZ in three regions, illustrated in the inset of Fig. 1 (e), and labeled X, Y, and Z. In each region, the non-equilibrium phonon populations are described via Bose-Einstein distributions $n_{\nu}(T_{\nu}) = [e^{\hbar\omega_{\nu}/k_{\text{B}}T_{\nu}} - 1]^{-1}$, with effective temperature T_{ν} and $\nu = \text{X, Y, Z}$. At each time t , the effective temperatures are determined by the solution of the coupled equations:

$$\begin{aligned} \frac{\partial T_{\text{el}}}{\partial t} &= \alpha \frac{I(t)}{c_{\text{el}}} - \sum_{\nu}^{\text{X,Y,Z}} \frac{g_{\nu}}{c_{\text{el}}} (T_{\text{el}} - T_{\nu}) \\ \frac{\partial T_{\nu}}{\partial t} &= \frac{g_{\nu}}{c_{\nu}} (T_{\text{el}} - T_{\nu}) - \sum_{\nu'}^{\text{X,Y,Z}} \frac{T_{\nu} - T_{\nu'}}{\tau_{\nu}} \end{aligned} \quad (2)$$

Here, $I(t)$ denotes a Gaussian laser pulse of duration $t_I = 50$ fs (see, e.g. Ref. [11]), whereas $\alpha = 5 \cdot 10^{-3}$ is the fraction of absorbed radiation from the black-phosphorus slab, τ_{ν} is the decay time of the phonon group ν . c_{el} is the electronic heat capacity, defined by:

$$c_{\text{el}}(T_{\text{el}}) = \int \frac{\partial f(\epsilon, \mu, T_{\text{el}})}{\partial T_{\text{el}}} F_{\text{el}}(\epsilon) \epsilon d\epsilon \quad (3)$$

with $F_{\text{el}}(\epsilon)$ being the electronic density of states. Similarly, the lattice heat capacity of the ν -th phonon group is given by:

$$c_{\nu}(T_{\nu}) = \hbar^2 \int \frac{\partial n_{\nu}(T_{\nu})}{\partial T_{\nu}} F_{\nu}(\omega) \omega d\omega, \quad (4)$$

where we introduced the partial density of states of the ν -th phonon group $F_{\nu}(\omega) = \Omega_{\nu}^{-1} \sum_{\mu} \int_{\Omega_{\nu}} d\mathbf{q} \delta(\hbar\omega - \hbar\omega_{\mu\mathbf{q}})$, with $\hbar\omega_{\mu\mathbf{q}}$ being the energy of the μ -th phonon with momentum \mathbf{q} , and Ω_{ν} is the volume of the ν -th region of the BZ.

The electron-phonon coupling coefficients are defined by:

$$g_{\nu} = \eta_{\nu} \frac{\pi k_{\text{B}}}{\hbar F_{\text{el}}(\mu_{\text{eff}})} \lambda \langle \omega^2 \rangle \int d\epsilon F_{\text{el}}^2(\epsilon) \left(-\frac{\partial f(\epsilon, \mu, T_{\text{el}})}{\partial T_{\text{el}}} \right), \quad (5)$$

where $\lambda \langle \omega^2 \rangle$ is the first moment of the Eliashberg spectral function, defined by:

$$\lambda \langle \omega^2 \rangle = 2 \int_0^{\infty} d\omega \omega \alpha^2 F(\omega). \quad (6)$$

The term $\eta_{\nu} = \int_{\Omega_{\nu}} d\mathbf{k} f(\epsilon, \mu, T_{\text{el}}) / \int_{\Omega_{\text{BZ}}} d\mathbf{k} f(\epsilon, \mu, T_{\text{el}})$ encodes information regarding occupation of electronic states in the different regions of the BZ. In practice, the inclusion of η_{ν} ensures that phonons with momenta in the ν -th region may be excited upon electron relaxation proportionally to the population of electronic state which may lead to such transition.

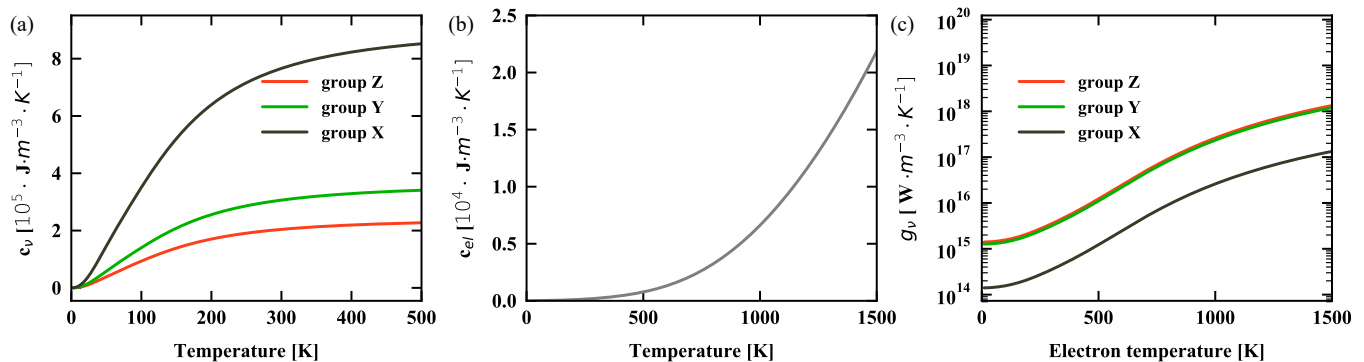
The values employed in the model are reported in supplementary Figure 4.

VI. COMPUTATIONAL DETAILS OF ELECTRON-PHONON AND PHONON-PHONON COUPLING CALCULATIONS.

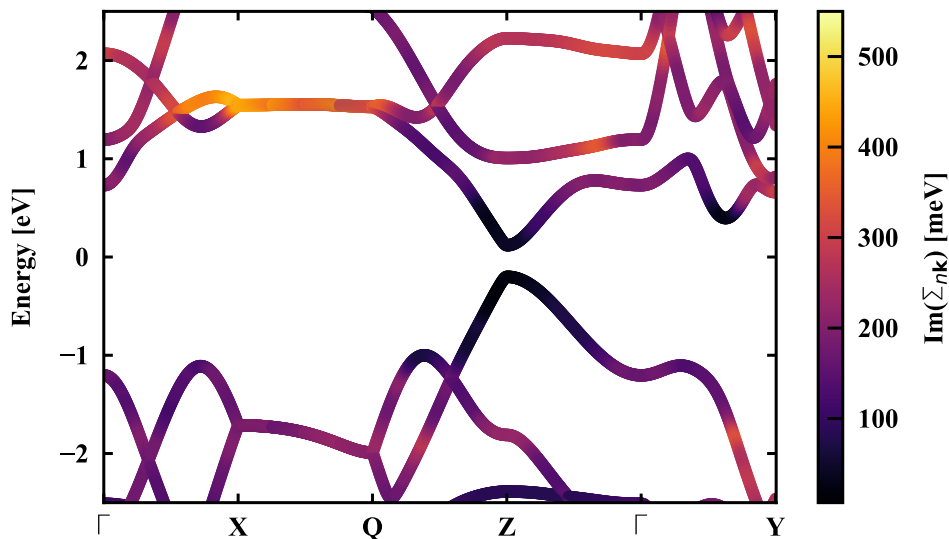
Equations (5) and (6) are evaluated from first-principles calculations of the electron-phonon interactions based on the EPW code [12]. Numerical details of the calculations are given below. Electronic and vibrational properties are computed based on density-functional and density-functional perturbation theory, as implemented in the plane-wave pseudo-potential code QUANTUM ESPRESSO [13], on a $8 \times 8 \times 8$ and $4 \times 4 \times 4$ homogeneous Monkhorst-Pack grids, respectively. All quantities are subsequently interpolated using maximally-localized Wannier functions on a random mesh consisting of 10000 \mathbf{k} points (100 \mathbf{q} points).

The imaginary part of the electron-phonon self-energy is shown in supplementary Figure 5 over a high-symmetry path for illustrative purposes.

The imaginary part of the anharmonic phonon self-energy Γ_{λ} has been obtained from first-principles calculations of the third-order force constants (3FC) as implemented in the `phono3py` package [14]. The 3FC has been computed by finite total-energy differences in a $2 \times 2 \times 2$ supercell. The average anharmonic phonon lifetime τ_0 is obtained phonon self-energy via $\tau_0 = N_{\lambda}^{-1} \sum_{\lambda}^{N_{\lambda}} (2\Gamma_{\lambda})^{-1}$. Finally, the time constant of each phonon group can be expressed by $\tau_{\nu} = N_{\lambda} \tau_0 \Omega_{\nu}^{-1} (\Omega_{\text{BZ}} - \Omega_{\nu})$.



Supplementary Figure 4. (a) Lattice heat capacities, c_ν , as defined in equation (4) for the three phonon groups as a function of temperature. (b) Electronic heat capacity, c_{el} , as defined in equation (3) as a function of temperature. (c) Electron-phonon coupling constants, g_ν , as defined in equation (5) for the three phonon groups as a function of electronic temperature.



Supplementary Figure 5. Electron linewidths due to the electron-phonon interaction as obtained from first principles calculations of the Fan-Migdal self-energy Σ_{nk} .

VII. REFERENCES

-
- [1] H. Jiang, H. Shi, X. Sun, and B. Gao, *ACS Photonics* **5**, 2509 (2018).
 - [2] H. B. Ribeiro, M. A. Pimenta, and C. J. de Matos, *Journal of Raman Spectroscopy* **49**, 76 (2018).
 - [3] J. P. Perdew, K. Burke, and M. Ernzerhof, *Phys. Rev. Lett.* **77**, 3865 (1996).
 - [4] N. Troullier and J. L. Martins, *Phys. Rev. B* **43**, 1993 (1991).
 - [5] P. Giannozzi, S. Baroni, N. Bonini, M. Calandra, R. Car, C. Cavazzoni, D. Ceresoli, G. L. Chiarotti, M. Cococcioni, I. Dabo, A. Dal Corso, S. de Gironcoli, S. Fabris, G. Fratesi, R. Gebauer, U. Gerstmann, C. Gougoussis, A. Kokalj, M. Lazzeri, L. Martin-Samos, N. Marzari, F. Mauri, R. Mazzarello, S. Paolini, A. Pasquarello, L. Paulatto, C. Sbraccia, S. Scandolo, G. Sclauzero, A. P. Seitsonen, A. Smogunov, P. Umari, and R. M Wentzcovitch, *J. Phys.: Condens. Matter* **21**, 395502 (2009).
 - [6] S. Baroni, S. de Gironcoli, A. Dal Corso, and P. Giannozzi, *Rev. Mod. Phys.* **73**, 515 (2001).

- [7] V. Vand, P. F. Eiland, and R. Pepinsky, *Acta Crystallographica* **10**, 303 (1957).
- [8] L.-M. Peng, S. Dudarev, and M. Whelan, *High-energy Electron Diffraction and Microscopy* (Oxford University Press, 2004).
- [9] A. A. Maradudin, E. W. Montroll, and G. H. Weiss, *Theory of lattice dynamics in the harmonic approximation* (Academic Press, New York, 1963) p. 240.
- [10] L. P. R. de Cotret, M. R. Otto, M. J. Stern, and B. J. Siwick, *Advanced Structural and Chemical Imaging* **4** (2018).
- [11] F. Caruso, D. Novko, and C. Draxl, *Phys. Rev. B* **101**, 035128 (2020).
- [12] S. Ponc e, E. Margine, C. Verdi, and F. Giustino, *Comp. Phys. Commun.* **209**, 116 (2016).
- [13] P. Giannozzi, O. Andreussi, T. Brumme, O. Bunau, M. B. Nardelli, M. Calandra, R. Car, C. Cavazzoni, D. Ceresoli, M. Cococcioni, *et al.*, *Journal of Physics: Condensed Matter* **29**, 465901 (2017).
- [14] A. Togo, L. Chaput, and I. Tanaka, *Phys. Rev. B* **91**, 094306 (2015).